

Series mixing in high- L Rydberg states of H_2 : An experimental test of polarization-model predictions

P. W. Arcuni, E. A. Hessels, and S. R. Lundeen

Department of Physics, University of Notre Dame, Notre Dame, Indiana 46556

(Received 13 September 1989)

Microwave spectroscopy of high- L $(0,1)nL_N$ Rydberg states of H_2 , with $26 \leq n \leq 30$ is reported. The results show a strong perturbation at $n=28$ due to the nearly degenerate $(0,3)16L_N$ states. Mixing between members of these two Rydberg series results in energy perturbations that can be measured quite precisely ($\leq 1\%$) from the microwave spectra and that are found to be in good agreement with *a priori* predictions based on the interseries matrix elements of the polarization potential. The connection between this use of the polarization potential and the systematic derivation of the polarization model from perturbation theory is discussed.

I. INTRODUCTION

The spectroscopy of high- L Rydberg states of H_2 has recently been studied with high resolution, using microwave resonance techniques.¹ The availability of these precise measurements increases the interest in the precise calculation of the level structure using the "polarization model,"² an approach designed to imitate the successful treatment of high- L states of the helium atom.³ In this model, only *long-range* nonhydrogenic interactions between the Rydberg electron and the H_2^+ ion core are considered, and these are expressed in terms of a "polarization potential" seen by the Rydberg electron. In lowest order this potential is

$$V_{\text{pol}}^{\text{LOPM}} = -\frac{eQ(\rho)}{r^3}P_2(\cos\theta) - \frac{e^2\alpha_S(\rho)}{2r^4} - \frac{e^2\alpha_T(\rho)}{3r^4}P_2(\cos\theta), \quad (1)$$

where r is the Rydberg electron's radial coordinate, LOPM represents the lowest-order polarization model, ρ is the internuclear separation of the H_2^+ ion core, and θ is the angle between the Rydberg electron's position and the direction of the internuclear axis. Q is the quadrupole moment. α_S and α_T are the isotropic and anisotropic dipole polarizabilities of the H_2^+ core. All three are functions of the internuclear separation. Additional terms in this polarization potential are in general proportional to higher inverse powers of r , and include higher static multipole terms and both adiabatic and nonadiabatic polarization terms. The coefficient of each term in the potential, e.g., $Q(\rho)$, $\alpha_S(\rho)$, etc., is a property of the free H_2^+ ion.

By the term "Rydberg state" we refer to a state where the H_2^+ core is in its ground electronic state. A particular Rydberg state is specified by the additional quantum numbers (ν, R) , the vibrational and rotational quantum numbers of the core, (n, L) , the principal and orbital angular momentum quantum numbers of the Rydberg electron, and by $\mathbf{N} = \mathbf{R} + \mathbf{L}$, the total angular momentum (ex-

clusive of spin). The set of all states differing only in the value of n is called a Rydberg series. It can be shown (see Sec. II below) that the energy of a particular Rydberg state R can be written in terms of the polarization potential V_{pol} as

$$E_R - E_R^0 = \langle \psi_R | V_{\text{pol}} | \psi_R \rangle + \sum_{R'} |\langle \psi_R | V_{\text{pol}} | \psi_{R'} \rangle|^2 / (E_R^0 - E_{R'}^0) + \dots, \quad (2)$$

where R' denotes all Rydberg states other than R . The expectation value of V_{pol} in a given Rydberg state, the first term in Eq. (2), gives the major portion of the quantum defect of that state. Interactions between different Rydberg series are represented by the second term of Eq. (2). These interactions, which dominate the structure of low- L H_2 Rydberg states,⁴ are much less significant for the high- L states. For instance, in the $(0,1)10L_N$ states studied in Ref. 1, the ratio between the first and second terms in Eq. (2) is calculated to be about 16 for $L=4$, and increases to about 150 for $L=7$. Equation (2) implies that the degree of mixing between Rydberg states in different series is directly predicted by the matrix elements of V_{pol} between the states in question.

A direct test of this prediction would be desirable. While not the dominant contribution to the Rydberg spectroscopy, the mixing terms are significant. The precise comparison between experimental measurement and theoretical prediction of $n=10$ Rydberg fine structure, described in Ref. 1, relies on the calculation of these mixing terms. Also, series mixing between discrete Rydberg levels is the bound-bound analog of the long-range autoionization process discussed by Eyler,⁵ which is not yet completely tested by experiment.

Although mixing between different high- L Rydberg series is generally quite small, near coincidences between the energies of Rydberg states in different series can lead to larger mixing. Under these circumstances, corresponding to an abnormally small energy denominator in the second term of Eq. (2), the mixing effects can lead to significant changes in the Rydberg state energies. Such is

the case for the $(0,1)28L_N$ and $(0,3)16L_N$ Rydberg states of H_2 , whose zeroth-order energies differ by about 0.25 cm^{-1} . Study of the energy shifts in the $n=28$ Rydberg levels, which we report here, provides the opportunity to test experimentally the degree of mixing predicted by the polarization model.

Using an extension of the experimental method used in Ref. 1, we have directly measured Rydberg fine-structure intervals in $(0,1)nL_N$ states with $26 \leq n \leq 30$ and $4 \leq L \leq 7$. This systematic study reveals the large perturbation of the electric-fine-structure pattern in the $(0,1)28L_N$ levels, which is caused by the perturbing $(0,3)16L_N$ levels. By extrapolating from the measured fine-structure intervals of the (nearly) unperturbed $n=26$, 27, 29, and 30 states to $n=28$, and subtracting the result from the measured $n=28$ fine-structure intervals, the shifts in the four $n=28$ fine-structure intervals are determined. The measured shifts are compared with *a priori* predictions which are obtained from the polarization model. Within the estimated errors of the model (which are obtained from the convergence of the polarization series) the comparison reveals good agreement.

In Sec. II below, the formulation of the polarization model is reviewed and extended to treat the mixing terms which involve higher-order terms in V_{pol} . The results are applied to predict the fine structure expected in the $26 \leq n \leq 30$ Rydberg states under study. Section III discusses the experimental measurements of the high- n fine-structure intervals. Section IV discusses the analysis of the measurements that are used to deduce the *shift* of each fine-structure integral at $n=28$, and compares these results with the predictions of the polarization model.

II. THEORY

The polarization model is derived from a perturbative solution of the nonrelativistic Schrödinger equation for H_2 , subject to two basic assumptions:

(i) The two electrons are distinguishable (electron 2 is the Rydberg electron).

(ii) The Rydberg electron is nonpenetrating. In what follows, a choice of coordinates slightly different from that of Ref. 2 is made, following the treatment of Drachman for high- L helium Rydberg states.⁶ In terms of the coordinates of the two protons ($\mathbf{R}_1, \mathbf{R}_2$) and the two electrons (r_{e_1}, r_{e_2}), the center of mass and relative coordinates are defined as

$$\mathbf{R}_C = (M\mathbf{R}_1 + M\mathbf{R}_2 + m\mathbf{r}_{e_1} + m\mathbf{r}_{e_2}) / (2M + 2m), \quad (3a)$$

$$\boldsymbol{\rho} \equiv \mathbf{R}_2 - \mathbf{R}_1, \quad (3b)$$

$$\mathbf{r}_1 \equiv \mathbf{r}_{e_1} - (\mathbf{R}_1 + \mathbf{R}_2) / 2, \quad (3c)$$

$$\mathbf{r}_2 \equiv \mathbf{r}_{e_2} - (M\mathbf{R}_1 + M\mathbf{R}_2 + m\mathbf{r}_{e_1}) / (2M + m), \quad (3d)$$

where M and m are the proton and electron masses. The three relative coordinates are Jacobi coordinates⁶ in that each gives the displacement of a single additional particle from the center of mass of a previously defined set of particles. By repeated use of the two-particle result

$$\frac{|\mathbf{p}_1|^2}{2m_1} + \frac{|\mathbf{p}_2|^2}{2m_2} = \frac{|\mathbf{P}_C|^2}{2M_T} + \frac{|\mathbf{p}|^2}{2\mu}, \quad (4)$$

where \mathbf{P}_C is the center-of-mass momentum and \mathbf{p} the relative momentum of the two-particle system, $M_T = m_1 + m_2$, and $\mu = m_1 m_2 / M_T$, it is easily shown that the total kinetic energy of the four-particle system H_2 can be written

$$E_{\text{kin}} = \frac{|\mathbf{P}_C|^2}{2M_T} + \frac{|\mathbf{P}_\rho|^2}{M} + \frac{|\mathbf{p}_1|^2}{2\mu_1} + \frac{|\mathbf{p}_2|^2}{2\mu_2}, \quad (5)$$

where $M_T = 2(M + m)$, $\mu_1 = m(1 - \epsilon)$, and $\mu_2 = m / (1 + \epsilon)$, with $\epsilon \equiv m / (2M + m)$. In Eq. 5, the successive momenta represent derivatives with respect to the four coordinates defined in Eq. (3). Thus, with this choice of coordinates, in contrast to the choice of Ref. 2, no "mass polarization" terms occur in the expression for the kinetic energy. However, the potential energy terms appear slightly more complex in this set of coordinates. Neglecting the center-of-mass coordinate, which separates, the complete Hamiltonian can be written

$$H = H_0 + V, \quad (6)$$

and

$$H_0 = \left[\frac{|\mathbf{P}_\rho|^2}{M} + \frac{|\mathbf{p}_1|^2}{2\mu_1} - \frac{e^2}{|\mathbf{r}_1 - \boldsymbol{\rho} / 2|} - \frac{e^2}{|\mathbf{r}_1 + \boldsymbol{\rho} / 2|} + \frac{e^2}{|\boldsymbol{\rho}|} \right] + \left[\frac{|\mathbf{p}_2|^2}{2\mu_2} - \frac{e^2}{|\mathbf{r}_2|} \right], \quad (7a)$$

$$V = \left[\frac{e^2}{|\mathbf{r}_2|} + \frac{e^2}{|\mathbf{r}_2 - \mathbf{r}_1 + \epsilon \mathbf{r}_1|} - \frac{e^2}{|\mathbf{r}_2 - \boldsymbol{\rho} / 2 + \epsilon \mathbf{r}_1|} - \frac{e^2}{|\mathbf{r}_2 + \boldsymbol{\rho} / 2 + \epsilon \mathbf{r}_1|} \right]. \quad (7b)$$

H_0 is the sum of the Hamiltonians of a free H_2^+ ion and of a hydrogen atom. Thus, the zeroth-order eigenstates are products of eigenstates for these two systems. In the Born-Oppenheimer (or adiabatic) approximations⁷ the wave functions for H_2^+ are written

$$\phi_{\alpha\Lambda\nu R m_r}^0(\boldsymbol{\rho}, \mathbf{r}_1) = \frac{g_{\alpha\Lambda\nu R}(\rho)}{\rho} \left[\frac{2R+1}{4\pi} \right]^{1/2} \times D_{\Lambda, m_r}^R(\hat{\boldsymbol{\rho}}) f_{\alpha\Lambda}(\mathbf{r}'_1; \rho). \quad (8)$$

The function $f_{\alpha\Lambda}(\mathbf{r}'_1; \rho)$ is the electronic wave function of the core electron in the molecule fixed frame, with quantum numbers Λ , which is associated with the operator $\mathbf{L}_1 \cdot \hat{\boldsymbol{\rho}}$, and α , which denotes all other electronic quantum numbers. The function $g_{\alpha\Lambda\nu R}(\rho)$ is the rovibrational wave function with vibrational quantum number ν and angular momentum R . $D_{\Lambda, m_r}^R(\hat{\boldsymbol{\rho}})$ is an element of the $(2R+1)$ -dimensional representation of the finite rotation that takes $\hat{\mathbf{z}}$ into $\hat{\boldsymbol{\rho}}$; by convention the third Euler angle is taken to be zero. A convenient zeroth-order basis for high- L Rydberg states is composed of linear combinations of product functions which diagonalize $\mathbf{N} = \mathbf{L} + \mathbf{R}$,

where \mathbf{L} is the angular momentum of electron 2. These are

$$\begin{aligned} \phi_{\alpha\Lambda\nu RnLN}^0(\boldsymbol{\rho}, \mathbf{r}_1, \mathbf{r}_2) \\ = \sum_{m_r, m_l} \langle Rm_r Lm_l | RLNM \rangle \phi_{\alpha\Lambda\nu Rm_r}^0(\boldsymbol{\rho}, \mathbf{r}_1) \phi_{nLm_l}^0(\mathbf{r}_2). \end{aligned} \quad (9)$$

Applying standard nondegenerate Rayleigh-Schrödinger perturbation theory, the energy of a given state can be expanded as

$$E(i) = E_i^0 + E_i^{[1]} + E_i^{[2]} + E_i^{[3]} + E_i^{[4]} + \dots, \quad (10a)$$

where

$$E_i^0 \equiv E^0(\alpha\Lambda\nu R) + E^0(n), \quad (10b)$$

$$E_i^{[1]} = \langle \phi_i^0 | V | \phi_i^0 \rangle, \quad (10c)$$

$$E_i^{[2]} = \sum_{j(\neq i)} \frac{|\langle \phi_i^0 | V | \phi_j^0 \rangle|^2}{(E_i^0 - E_j^0)}, \quad (10d)$$

$$E_i^{[3]} = \sum_{j,k(\neq i)} \frac{\langle \phi_i^0 | V | \phi_j^0 \rangle \langle \phi_j^0 | V | \phi_k^0 \rangle \langle \phi_k^0 | V | \phi_i^0 \rangle}{(E_i^0 - E_j^0)(E_i^0 - E_k^0)} \quad (10e)$$

$$- \langle \phi_i^0 | V | \phi_i^0 \rangle \sum_{j(\neq i)} \frac{\langle \phi_i^0 | V | \phi_j^0 \rangle \langle \phi_j^0 | V | \phi_i^0 \rangle}{(E_i^0 - E_j^0)^2}, \quad (10f)$$

$$E_i^{[4]} = \sum_{j,k,l(\neq i)} \frac{\langle \phi_i^0 | V | \phi_j^0 \rangle \langle \phi_j^0 | V | \phi_k^0 \rangle \langle \phi_k^0 | V | \phi_l^0 \rangle \langle \phi_l^0 | V | \phi_i^0 \rangle}{(E_i^0 - E_j^0)(E_i^0 - E_k^0)(E_i^0 - E_l^0)} \quad (10g)$$

$$- 2 \langle \phi_i^0 | V | \phi_i^0 \rangle \sum_{j,k(\neq i)} \frac{\langle \phi_i^0 | V | \phi_j^0 \rangle \langle \phi_j^0 | V | \phi_k^0 \rangle \langle \phi_k^0 | V | \phi_i^0 \rangle}{(E_i^0 - E_j^0)(E_i^0 - E_k^0)^2} \quad (10h)$$

$$+ |\langle \phi_i^0 | V | \phi_i^0 \rangle|^2 \sum_{j(\neq i)} \frac{\langle \phi_i^0 | V | \phi_j^0 \rangle \langle \phi_j^0 | V | \phi_i^0 \rangle}{(E_i^0 - E_j^0)^3} \quad (10i)$$

$$- \sum_{j(\neq i)} \frac{|\langle \phi_i^0 | V | \phi_j^0 \rangle|^2}{(E_i^0 - E_j^0)} \sum_{k(\neq i)} \frac{|\langle \phi_i^0 | V | \phi_k^0 \rangle|^2}{(E_i^0 - E_k^0)^2}. \quad (10j)$$

In Eq. (10) it is tacitly assumed that the zeroth-order states are nondegenerate, while actually Rydberg levels that have the same quantum numbers ν , R , and n are degenerate in zeroth order. If this formal difficulty is ignored, however, it is possible to relate the results obtained from Eq. (10) with the eigenvalues of an effective Hamiltonian which acts in the subspace of Rydberg states. In this interpretation the problem of divergent energies from coupling of degenerate levels, in Eq. (2), is removed. It is also true that V is nearly diagonal in the $(\nu, R)nL_N$ basis, at least for high- L states. As discussed below, the lowest nonzero multipole moment of V that can potentially couple degenerate states is the quadrupole

term, which may couple basis states with $\Delta L = 2$. These matrix elements are zero, however, since the matrix element of r_2^{-3} between hydrogenic radial functions of common n , but differing in L by 2, are exactly zero.⁸ The remaining higher-order nonzero couplings are quite small.

If, for the present, terms of order ϵ in V are neglected,⁹ then setting $\epsilon = 0$ in Eq. (7b) and assuming no penetration ($r_2 > r_1$, $r_2 > \rho/2$), the perturbation V in Eq. (10) may be expanded in a multipole series

$$V = \sum_{\kappa=1}^{\infty} V^{[\kappa]} \equiv \sum_{\kappa=1}^{\infty} \left[\frac{r_1^{\kappa}}{r_2^{\kappa+1}} P_{\kappa}(\cos\theta_{21}) - [1 + (-1)^{\kappa}] \frac{(\rho/2)^{\kappa}}{r_2^{\kappa+1}} P_{\kappa}(\cos\theta_{2\rho}) \right]. \quad (11)$$

Successive terms in this expansion are expected to converge rapidly, each being smaller by an additional factor r_1/r_2 , the ratio of core size to Rydberg orbit size. This convergence may be used to estimate the approximate size of contributions to $E(i)$ from each term in Eq. (10). It is advantageous to divide the set of all eigenstates of H_0 into two subsets. One set R is the set of all Rydberg states, defined by the fact that the core electron is in its ground electronic state. The other set U contains all other eigenstates of H_0 . Each of the sums occurring in Eq. (10) may be separated into a sum over R and a sum over U . Since the core electronic state is an eigenstate of electronic parity (g/u), the perturbation $V^{[\kappa]}$ has nonzero matrix elements *within* R only if κ is even.

In order to make the correspondence between the polarization model [Eq. (2)] and the perturbation expansion of the full Hamiltonian [Eq. (10)], we may collect the terms of Eq. (10) into three classes: (i) terms having *no* Rydberg-Rydberg energy denominator, (ii) terms having *one* Rydberg-Rydberg energy denominator, and (iii) terms having more than one Rydberg-Rydberg energy denominator. Terms of class (i) will contribute to the first term in Eq. (2), terms from class (ii) to the second, and terms from class (iii) would represent terms of higher order in V_{pol} . Within each class, the approximate magnitude of each multipole term in Eq. (10) can be estimated by using the two rules

$$\langle \phi_i^0 | V^{[\kappa]} | \phi_j^0 \rangle \cong \frac{e^2}{r_2} (r_1/r_2)^{\kappa},$$

$$E_i^0 - E_j^0 \cong \frac{e^2}{r_1}, \quad \text{unless } i \text{ and } j \text{ are both in } R.$$

In these expressions, r_1 and r_2 are parameters representing the approximate radial scale of the core and Rydberg electron wave function. Table I lists the most important terms obtained from Eq. (10) and identifies them with terms obtained by applying V_{pol} in Eq. (2).

In addition to the expansions represented by Eqs. (10) and (11), one additional expansion is advantageous to the calculation. Whenever an energy denominator includes a core excitation energy, that energy is assumed to dom-

inate the energy difference, and the full term is expanded in the ratio of Rydberg to core excitation energies,

$$\begin{aligned} & [E^0(\alpha\Lambda\nu Rn) - E^0(\alpha'\Lambda'\nu'R'n')]^{-1} \\ & \cong [E^0(\alpha\Lambda\nu R) - E^0(\alpha'\Lambda'\nu'R')]^{-1} \\ & \quad - [E^0(n) - E^0(n')] \\ & \quad \times [E^0(\alpha\Lambda\nu R) - E^0(\alpha'\Lambda'\nu'R')]^{-2} \dots \quad (12) \end{aligned}$$

The first term of Eq. (12) leads to the “adiabatic” polarization energies, while the second term gives the first “nonadiabatic” polarization terms. The calculation of

$$\begin{aligned} V_{\text{pol}}^{\text{HOPM}} = V_{\text{pol}}^{\text{LOPM}} - \frac{e\phi(\rho)}{r^5} P_4(\cos\theta) - \frac{e^2}{r^6} \left[\frac{C_0(\rho)}{10} + \frac{C_1(\rho)}{7} P_2(\cos\theta) + \frac{12C_2(\rho)}{35} P_4(\cos\theta) \right] \\ + \frac{e^4 a_0}{r^6} \left[\frac{3}{2} \beta_S(\rho) + \frac{1}{2} \beta_T(\rho) P_2(\cos\theta) \right] - \frac{e^2}{r^6} \left[\frac{1}{7} E_1(\rho) P_2(\cos\theta) + \frac{1}{35} E_2(\rho) P_4(\cos\theta) \right], \quad (13) \end{aligned}$$

where $\phi(\rho)$ is the electric hexadecapole moment of H₂⁺, C_0 , C_1 , and C_2 are the spherical components of the adiabatic quadrupole polarizability, β_S and β_T are the scalar and tensor components of the first nonadiabatic dipole polarizability, and E_1 and E_2 are spherical components of the adiabatic dipole-octupole polarizability.² Similarly, the largest terms in class II are obtained when $V_{\text{pol}}^{\text{HOPM}}$ is substituted into the second term of Eq. (2), and the cross terms grouped according to the “total” power of r_2 . These are the terms which describe energy shifts due to mixing between different Rydberg series. Only the largest of these was discussed in Ref. 2. Many of the others

the dipole polarization terms of both types is described in detail elsewhere.^{2,10} In that case it is found that the nonadiabatic terms are smaller than the adiabatic by two additional powers of r_1/r_2 , as indicated in Table I. The detailed correspondence between the specific terms of Eqs. (2) and (10), as indicated in Table I, may be confirmed term by term¹⁰ using methods similar to those of Ref. 2.

As Table I illustrates, the largest terms of class I are just those terms included in the higher-order polarization model² (HOPM). In this approximation, the terms included in V_{pol} , in addition to Eq. (1), are

originate in third- or fourth-order perturbation expressions of V , shown in Eq. (10), which were not considered there. Terms in either class I or class II which are not included in Table I can be demonstrated to be of higher order in the parameter r_1/r_2 , and are expected to be correspondingly less significant.

One advantage of calculating Rydberg state energies with the polarization model is that the rate of convergence of the polarization series gives a natural way to estimate the probable error in the estimate due to neglect of even higher-order terms. Following Drachman,³ the total contribution of all terms proportional to r^{-5} is denot-

TABLE I. Identification of the polarization model expressions for Rydberg state energy with the perturbation-theory expressions of Eq. (10). Terms in class I have no Rydberg intermediate states, while those in class II have one intermediate Rydberg state. The notation (10d) ($j \subset R$) indicates that the intermediate state j of Eq. (10d) is a Rydberg state. Whenever it is not explicitly stated, it is assumed that the relevant intermediate states are *not* Rydberg states. The indices κ_i refers to the multipole expansion of the perturbation V [Eq. (11)]. When more than one index κ occur, they refer to different occurrences of V in Eq. (10), read from left to right.

Class I					V_{pol} term	
Equation	κ_1	κ_2	Magnitude			
(10c)	2		$(e^2/r_2)(r_1/r_2)^2$	Q : static quadrupole potential		
(10d)	1	1	$(e^2/r_2)(r_1/r_2)^3$	α : adiabatic dipole polarizability		
(10c)	4		$(e^2/r_2)(r_1/r_2)^4$	ϕ : static hexadecapole potential		
(10d)	1 ^a	1	$(e^2/r_2)(r_1/r_2)^5$	β : nonadiabatic dipole polarizability		
(10d)	2	2	$(e^2/r_2)(r_1/r_2)^5$	C : adiabatic quadrupole polarizability.		
(10d)	1	3	$(e^2/r_2)(r_1/r_2)^5$	E : adiabatic dipole-octupole polarizability.		
Class II						
Equation	κ_1	κ_2	κ_3	κ_4	Numerator magnitude	V_{pol} term
(10d) ($j \subset R$)	2	2			$(e^2/r_2)^2(r_1/r_2)^4$	Q - Q mixing
(10e) ($k \subset R$)	1	1	2		$(e^2/r_2)^2(r_1/r_2)^5$	α - Q mixing
(10d) ($j \subset R$)	2	4			$(e^2/r_2)^2(r_1/r_2)^6$	Q - ϕ mixing
(10g) ($k \subset R$)	1	1	1	1	$(e^2/r_2)^2(r_1/r_2)^6$	α - α mixing
(10e) ($k \subset R$)	1	1	4		$(e^2/r_2)^2(r_1/r_2)^7$	α - ϕ mixing
(10e) ($k \subset R$)	2	2	2		$(e^2/r_2)^2(r_1/r_2)^7$	C - Q mixing
(10e) ($k \subset R$)	1	3	2		$(e^2/r_2)^2(r_1/r_2)^7$	E - Q mixing
(10e) ($k \subset R$)	1 ^a	1	2		$(e^2/r_2)^2(r_1/r_2)^7$	β - Q mixing

^aNotation indicates the first nonadiabatic correction to the $\kappa=1$ term from Eq. (12).

ed V_s . We can estimate the two terms of Eq. (2) using only the terms included in $V_{\text{pol}}^{\text{HOPM}}$,

$$\langle \psi_R | V_{\text{pol}} | \psi_R \rangle \cong V_3 + V_4 + V_6/2 \pm V_6/2, \quad (14)$$

where it has been assumed that V_6 is the smallest contribution. Similarly, the second term of Eq. (2) may be estimated

$$\sum_{R'} \frac{|\langle \psi_R | V_{\text{pol}} | \psi_{R'} \rangle|^2}{E_R^0 - E_{R'}^0} \cong V_6 + V_7 + V_8 + V_9 \pm V_9/2, \quad (15)$$

where V_s denotes the total of all cross terms with "total" power of r_2 equal to $-s$. The different treatment of the smallest term is due to the fact that successive contributions to Eq. (14) are observed to alternate in sign while this is not true for Eq. (15).

Finally, the largest term from class III is obtained from Eqs. (10e) and (10f) when both j and k being to R and $\kappa_1 = \kappa_2 = \kappa_3 = 2$. This term does not contribute to either of the two terms of Eq. (2). However the expression of Eq. (2) can be recognized as the first two perturbation orders in the expansion of the eigenvalues of the matrix $H_0 + V_{\text{pol}}$, defined in the space of Rydberg states. The term in question here, the largest term of class III, is identical to the lowest-multipole part of the third-order extension of Eq. (2). Recognizing this, we may hypothesize that the correct energy for Rydberg levels, to all orders in V_{pol} , is found simply by diagonalizing the matrix of

$$H_{\text{eff}} = H_0 + V_{\text{pol}} \quad (16)$$

within the space of Rydberg states. We must stress the somewhat tentative character of this hypothesis, which interprets $H_0 + V_{\text{pol}}$ as an effective Hamiltonian. There has been no formal proof justifying such an interpretation. Although the result is similar to that obtained elsewhere by rigorous arguments,¹¹ the conditions of that proof do not seem to apply here, in particular, the space of Rydberg levels is not well isolated from the other states of the H_2 molecule. On the other hand, the hypothesis is plausible and in agreement with experiment, as will be seen later.

The interpretation of V_{pol} as part of an effective Hamiltonian removes the formal difficulty associated with mixing of nominally degenerate zeroth-order states. Since the diagonal polarization energies remove this degeneracy, and are much larger than those matrix elements of

V_{pol} which mix these levels, the degree of mixing is generally small, and the energy shifts which result can easily be calculated. This interpretation also proves to be necessary when comparing calculations to our experimental data which measures perturbations between the (0,1)28 and (0,3)16 Rydberg levels, where the diagonal polarization energies are comparable to the differences between zeroth-order energies.

**Application to the (0,1) nL_N states of H_2 ,
with $26 \leq n \leq 30$ $4 \leq L \leq 6$**

Using the electrical properties which have been calculated for the (0,1) state of H_2^+ , listed in Appendix A, the fine structure of the (0,1) nL states can be predicted. Because of angular momentum factors, all terms in V_{pol} proportional to $P_4(\cos\theta)$ give zero contribution to the expectation value for these $R=1$ states. Consequently, the "first-order polarization energies," the first term of Eq. (2), can be written

$$\langle \psi_R | V_{\text{pol}} | \psi_R \rangle = A_0 + A_2 \langle RLN | P_2(\cos\theta) | RLN \rangle, \quad (17a)$$

where

$$\begin{aligned} & \langle RLN | P_2(\cos\theta) | RLN \rangle \\ &= \frac{3S(S-1) - 4L(L+1)R(R+1)}{2(2R-1)(2R+3)(2L-1)(2L+3)}, \quad (17b) \end{aligned}$$

with $S \equiv R(R+1) + L(L+1) - N(N+1)$. The calculated scalar (A_0) and tensor (A_2) structure factors for each of the states of concern here are given in Table II. The error bars are obtained from Eq. (14).

The "second-order polarization energies," the second term in Eq. (2), involve contributions from many Rydberg series which are coupled to the state in question by V_{pol} . Since V_{pol} is scalar, all nonzero couplings satisfy $\Delta N = 0$. The selection rules on R and L are determined by the dependence on θ , the angle between \hat{p} and \hat{r}_2 . The three types of angular dependence in Eq. (13) give the selection rules

$$\Delta R = 0, \quad \Delta L = 0 \quad \text{for } P_0(\cos\theta) = 1,$$

$$\Delta R = 0, \pm 2, \quad \Delta L = 0, \pm 2 \quad \text{for } P_2(\cos\theta),$$

$$\Delta R = 0, \pm 2, \pm 4, \quad \Delta L = 0, \pm 2, \pm 4 \quad \text{for } P_4(\cos\theta).$$

TABLE II. Scalar and tensor structure factors for some (0,1) nL Rydberg states. All values are in MHz. The numbers in parentheses include convergence errors only.

Factor	n					
	26	27	28	29	30	
$A_0(G)$	-497(13)	-445(11)	-399(10)	-359(9)	-325(8)	
$A_0(H)$	-180(2)	-161(2)	-144.7(15)	-130.4(13)	-117.8(11)	
$A_0(I)$	-77.2(4)	-69.1(3)	-62.0(3)	-55.9(3)	-50.5(2)	
$A_2(G)$	-7250(7)	-6474(6)	-5805(6)	-5226(5)	-4720(5)	
$A_2(H)$	-3876(1)	-3462(1)	-3103.9(8)	-2793.9(7)	-2523.8(6)	
$A_2(I)$	-2315.8(2)	-2068.0(2)	-1854.3(2)	-1669.1(1)	-1507.7(1)	

Matrix elements between states of different vibrational quantum number ν are determined by the matrix elements of the core electronic moments, such as $Q(\rho)$ or $\alpha_S(\rho)$. Generally, these decrease as $\Delta\nu$ increases. These off-diagonal matrix elements have been tabulated for most cases of interest.¹²

In general, the calculated energy shift due to mixing from a given series of Rydberg levels arises from mixing with both bound and continuum members of the series. The shift due to bound levels has been estimated by explicitly evaluating the contributions of the lowest 45 members of each series and extrapolating to include, approximately, the rest of the bound levels. The energy shift due to coupling to continuum levels has been estimated by calculating the contributions of several representative continuum levels in the energy range $\epsilon=0$ to 0.6 a.u. For this purpose, the continuum radial wave functions were calculated by numerical integration of the Schrödinger equation and normalized to analytic hydrogenic wave functions at small r . In all cases studied, the contributions decreased smoothly at the largest continuum energies. The high-energy behavior was fit to a power-law function ($\Delta E \propto \epsilon^{-b}$) to estimate the integrated contribution.

Table III shows, for example, the calculated energy shifts of a particular Rydberg state, the $(0,1)26H_6$ state, caused by mixing with other series. Note that the shift due to coupling to the single state $(0,3)16H_6$ is listed separately and is small. This same perturbing state causes a large perturbation of the $(0,1)28H_6$ state, with which it is nearly degenerate. Also listed separately are the shifts due to coupling to the nominally "degenerate" states in the $(0,1)n=26$ manifold. These are also quite small. Table IV shows the total calculated shift for each of the 30 $(0,1)nL_N$ Rydberg levels of interest in this experiment.

TABLE III. Calculated energy shifts of the $(0,1)26H_6$ state due to coupling to other Rydberg series. The numbers in parentheses are derived from Eq. (16). When errors are not shown they are negligibly small when calculated by this prescription. All values are in MHz.

Series	Bound	Continuum	Total
$(0,1)nH_6$	1.329(7)	-2.245(13)	-0.916(15)
$(0,1)nK_6^a$	0.000	-2.400(1)	-2.400(1)
$(0,3)nF_6$	3.983(5)	-0.023(1)	3.960(6)
$(0,3)nH_6^b$	3.045	-2.998(2)	0.047(2)
$(0,3)nK_6$	0.000	-0.343(1)	-0.343(1)
$(1,1)nH_6$	0.117	-0.042	-0.159
$(1,1)nK_6$	0.000	-0.086	-0.086
$(1,3)nF_6$	0.344	-0.001	0.343
$(1,3)nH_6$	-0.076	-0.061	-0.137
$(1,3)nK_6$	0.000	-0.013	0.013
$(0,3)16H_6$	3.188		
$(0,1)26K_6$	0.038		

^aThe contribution from a "degenerate" level is tabulated separately.

^bThe single state $(0,3)16H_6$ is tabulated separately.

TABLE IV. Total second-order polarization energies calculated for the 30 Rydberg states of interest. Coupling to both discrete and continuum Rydberg levels is included, but coupling with the $(0,3)16L_N$ levels, which is very large for $n=28$, is excluded in all cases. The numbers in parentheses are estimated from Eq. (16). All results are in MHz.

State	Shift	State	Shift
$(0,1)26G_3$	-6.0(5)	$(0,1)26G_5$	-1.4(4)
$(0,1)27G_3$	-7.1(5)	$(0,1)27G_5$	-5.4(3)
$(0,1)28G_3$	-7.8(5)	$(0,1)28G_5$	-7.8(3)
$(0,1)29G_3$	-8.2(4)	$(0,1)29G_5$	-9.5(3)
$(0,1)30G_3$	-8.5(4)	$(0,1)30G_5$	-10.8(3)
$(0,1)26H_4$	-0.45(4)	$(0,1)26H_6$	0.26(3)
$(0,1)27H_4$	-0.80(3)	$(0,1)27H_6$	-0.79(3)
$(0,1)28H_4$	-1.11(3)	$(0,1)28H_6$	-1.43(10)
$(0,1)29H_4$	-1.34(3)	$(0,1)29H_6$	-1.93(2)
$(0,1)30H_4$	-1.51(3)	$(0,1)30H_6$	-2.29(2)
$(0,1)26I_5$	-0.051(3)	$(0,1)26I_7$	0.183(2)
$(0,1)27I_5$	-0.320(3)	$(0,1)27I_7$	-0.173(2)
$(0,1)28I_5$	-0.208(3)	$(0,1)28I_7$	-0.389(9)
$(0,1)29I_5$	-0.373(3)	$(0,1)29I_7$	-0.545(2)
$(0,1)30I_5$	-0.459(2)	$(0,1)30I_7$	-0.649(1)

III. EXPERIMENT

In order to study the spectroscopy of high- n Rydberg levels of H_2 with microwave methods, we devised an extension of the techniques described in Ref. 1, which was based on the ability to saturate the laser transitions from the $n=10$ to high- n states. The apparatus is shown schematically in Fig. 1. A beam of H_2^+ ions is extracted from a duoplasmatron ion source, accelerated to about 11 keV, and after mass selection in a bending magnet, neutralized in a charge-exchange cell containing a few millitorr of argon. A small portion of the fast neutral beam emerging from the charge exchange cell is in the $n=10$ Rydberg states of interest. After neutralization, the beam passes through a strong transverse electric field which deflects the remaining ions out of the beam and also Stark ionizes Rydberg levels with $n \geq 22$. A Doppler-tuned cw CO_2 laser then excites a particular $n=10$ Rydberg level to a specific high- n level, for instance, the $(0,1)10G_5$ to the $(0,1)27H_6$ level. The selection of this particular excitation transition from all possible 10-27 transitions is provided by the frequency resolution of the laser.¹³ The laser intensity ($\cong 5$ W/cm² and interaction time ($\cong 10$ nsec) are sufficient to saturate the transition in question. Further down the apparatus, as illustrated in Fig. 1, a second laser interaction region is encountered by the fast beam, also tuned to excite this *same* transition. Since this transition has already been saturated by the first laser, the second laser would be expected to have little effect on the Rydberg level populations. This is indeed the case if nothing intervenes to alter the populations in the time between the two lasers. If, however, resonant transitions are induced in the microwave region, located between the two lasers, which reduce the population of the upper state, the second laser *will* be able to excite additional molecules to the upper level. After the second laser in-

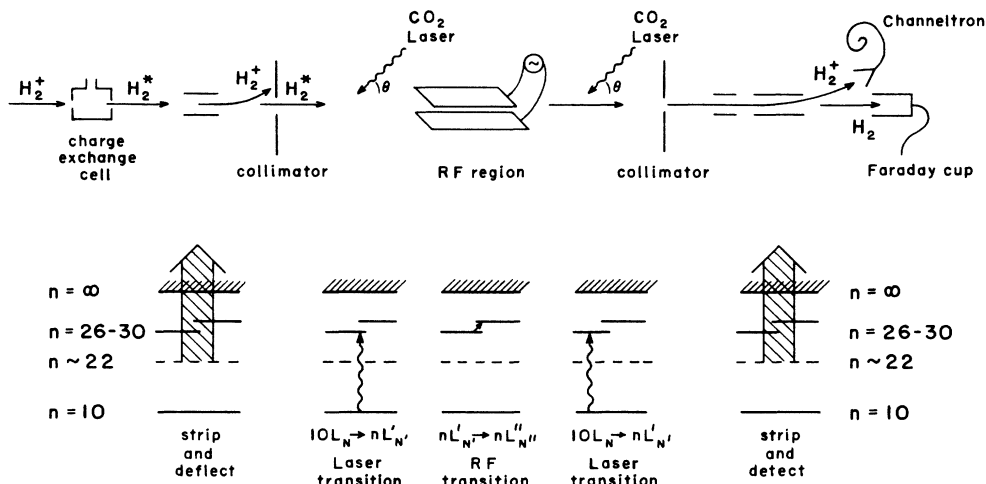


FIG. 1. A schematic diagram of the apparatus, with the induced level transitions shown below. Rydberg H_2 molecules are created from an 11-keV H_2^+ ion beam inside the charge-exchange cell. Those molecules in the $(0,1)10G_N$, $N=3$ or 5 , are then excited, inside the first laser interaction region, to a particular $(0,1)nH_N$ state, where $26 \leq n \leq 30$, $N=4$ or 6 . Microwave transitions connecting the upper level to other Rydberg states of the same n are induced in the rf transmission-line interaction region following the first laser. In the second laser interaction region the same $10G_N - nH_{N+1}$ transition is stimulated that was stimulated in the first laser interaction region. The number of additional excited states depends, however, on the effectiveness of the rf excitation in redistributing the upper-level states. Following the second laser all of the excited states are Stark ionized; the resulting ions are deflected into a channeltron electron multiplier. The rf resonance between large- n Rydberg states is observed by modulating the microwave intensity and measuring the synchronous modulation of the channeltron current. The resulting signal is measured as a function of the frequency applied to the rf transmission line.

teraction region, a strong electric field Stark ionizes all Rydberg levels with $n \geq 22$ and the resulting ions are deflected into a channeltron electron multiplier. The channeltron current is proportional to the total population of $n \geq 22$ Rydberg levels in the beam after the second laser. The effect of induced microwave transitions in the high- n state, therefore, is to increase the channeltron current, since in the absence of these induced transitions, fewer molecules would have been excited to the upper level.

Evidence that the laser excitation transition is indeed saturated is shown in Fig. 2. The plotted signal is the ac component of the channeltron current synchronous with a square wave modulation of the second laser's intensity, plotted as a function of the Doppler-tuned frequency of the first (unmodulated) laser. The positive signal observed over most of the plot occurs since the second laser is always tuned to the center of the $(0,1)10G_5 - (0,1)27H_6$ transition. When the first laser is also tuned to that transition, however, as at the center of Fig. 2, it saturates the transition and approximately equalizes the populations of upper and lower states, thus greatly reducing the effect of the second laser as indicated by the dip in the plotted signal. Actually, as Fig. 2 shows, the signal even changes sign when the first laser is tuned to the center of the line. This appears to be consistent with the creation of a population inversion by radiative decay during the time between the two lasers, which would be expected since the lower state has the shorter radiative lifetime.

It is worth noting that the above explanation of the processes responsible for the data of Fig. 2 completely neglects the possibility of redistribution of the upper-state populations in the time between the two lasers. Yet such

redistribution might occur in response to rather minor perturbations. Electric fields as small as 0.3 V/cm are sufficient to strongly mix the different Rydberg levels which share the same high n . Consequently, nonadiabatic motion through such a field would certainly redistribute the populations. Also, the cross section for population redistribution in gas phase collisions with neutral background gas ($P \cong 10^{-7}$ Torr) are probably on the or-

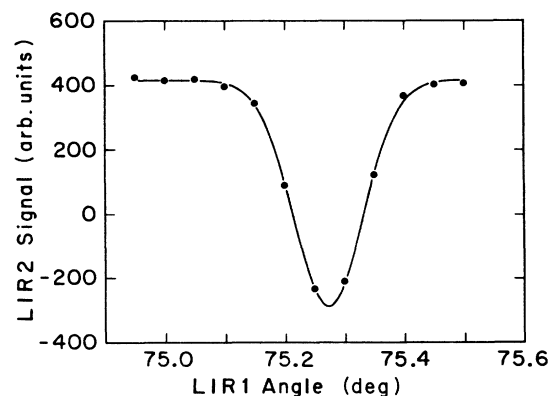


FIG. 2. Demonstration of the saturation of the laser excitation transition. The plotted signal is the ac component of the channeltron current that is synchronous with modulation of the intensity of the second laser. It is plotted as a function of the (Doppler-tuning) angle of the first (unmodulated) laser. When both lasers are tuned to the excitation transition, as at the center of the plot, the effect of the second laser is dramatically reduced, indicating that the first laser has saturated the transition.

der of $n^4 a_0^2$, which is close to the size that would be required for significant redistribution. Finally, the cross section for redistribution in collisions with charged particles¹⁴ is probably 2–3 orders of magnitude greater than $n^4 a_0^2$, which implies that any significant degree of ionization of the background gas or other source of charged particles could cause population redistribution. Nevertheless, such redistribution does *not* seem to occur in the experiment.

In order to observe the high- n fine-structure transition resonances, both lasers are tuned to the same excitation transition (at the “dip” in Fig. 2) and neither laser is modulated. Then a small microwave electric field is applied in the transmission line interaction region between the two lasers, with square-wave modulated amplitude. The component of the channeltron current synchronous with this modulation of the microwave intensity is then measured as a function of the microwave frequency. Two transitions are observed from each laser excited upper state. For instance, the $(0,1)10G_5-(0,1)27H_6$ laser transition allows the observation of the $(0,1)27G_5-(0,1)27H_6$ and the $(0,1)27H_6-(0,1)27I_7$ radio-frequency transitions. Typical observations of these two signals are shown in Fig. 3. The resonance linewidth, determined by the tran-

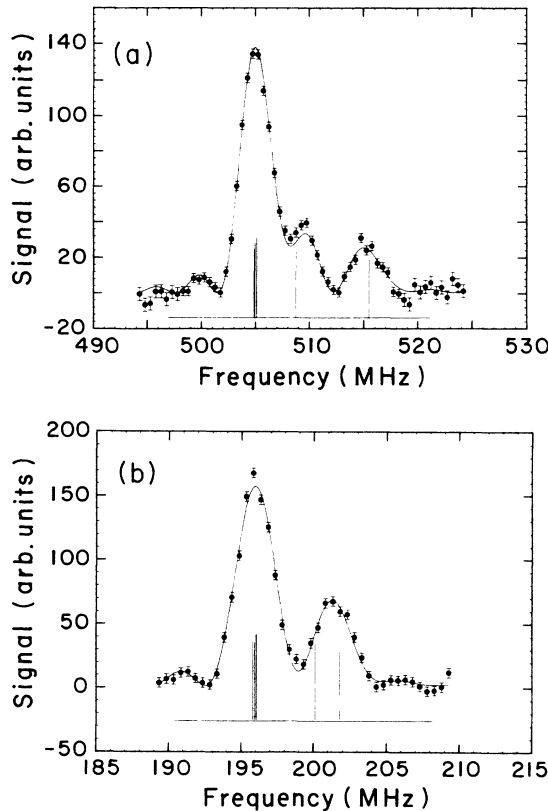


FIG. 3. Two examples of high- n fine-structure transitions observed in this experiment: (a) the $(0,1)27G_5-(0,1)27H_6$ transition, and (b) the $(0,1)27H_6-(0,1)27I_7$ transition. Both of these transitions can be observed when the lasers are tuned to excite the $(0,1)10G_5-(0,1)27H_6$ transition. The stick diagram shows the predicted substructure in the lines due to the magnetic fine structure of the levels, as discussed in the text. The smooth curves show fits of the data to a sum of six time and power broadened functions, also as discussed in the text.

sit time through the microwave field, is about 3.5 MHz for this data. This is small enough to reveal some substructure to the resonances, evident in Fig. 3, which can be attributed to the “magnetic fine structure” (MFS) of the Rydberg levels, as discussed below. When this is accounted for, each resonance may be fit to extract a single line center, referred to as the “electric-fine-structure” (EFS) interval and defined as the single interval which would be observed in the absence of all spins. This interval can be compared with the predictions of the polarization model, where all spins are ignored. Table V lists the 20 high- n transitions observed for this study, and gives the results of the fits to determine the EFS intervals. The fit procedure is discussed in detail below.

A. Magnetic fine structure

The finest level of structure in H_2 Rydberg states has been studied in the case of high- L $n=10$ levels¹⁵ where it has been found to be accounted for to a precision of at least 1% by the following *ad hoc* MFS Hamiltonian:

$$H_{\text{MFS}} = H_{\text{HFS}} + H_{\text{MS}} + (-1)^S V_x, \quad (18)$$

where H_{HFS} is the hyperfine Hamiltonian of the free H_2^+ ion,

$$H_{\text{HFS}} = b(\mathbf{I} \cdot \mathbf{S}_1) + c(\mathbf{I} \cdot \hat{\rho})(\hat{\rho} \cdot \mathbf{S}_1) + d(\mathbf{R} \cdot \mathbf{S}_1) \quad (19)$$

with \mathbf{I} denoting the total proton spin ($I=1$ for $R=1$

TABLE V. Experimental values of 20 high- n fine-structure intervals in H_2 . Column 1 identifies the interval, where $nL_N-L'_N$ is the interval between the $(0,1)nL_N$ and $(0,1)nL'_N$ states. Raw results of fits from experimental spectra are shown in column 2. Corrections for stray electric field (25 ± 10 mV/cm) are shown in column 3, with corrected results in column 4. All results are in MHz. The numbers in parentheses denote one standard deviation error estimates.

Interval	ν_0^{fit}	$\Delta\nu_0$	ν_0
$26G_3-H_4$	840.00(6)	0.21(15)	840.21(26)
$27G_3-H_4$	754.63(7)	0.27(20)	754.90(21)
$28G_3-H_4$	986.65(6)	0.08(20)	986.72(21)
$29G_3-H_4$	599.79(11)	0.45(30)	600.24(32)
$30G_3-H_4$	545.04(6)	0.58(40)	545.62(41)
$26G_5-H_6$	552.68(3)	0.30(20)	552.98(20)
$27G_5-H_6$	505.13(3)	0.39(30)	505.52(30)
$28G_5-H_6$	872.10(13)	0.38(25)	872.48(28)
$29G_5-H_6$	381.26(3)	0.64(45)	381.90(45)
$30G_5-H_6$	353.24(3)	0.81(50)	354.05(50)
$26H_4-I_5$	325.21(5)	0.32(20)	325.53(21)
$27H_4-I_5$	291.30(3)	0.42(30)	291.72(30)
$28H_4-I_5$	330.41(5)	0.52(40)	330.93(40)
$29H_4-I_5$	232.39(4)	0.72(50)	233.11(50)
$30H_4-I_5$	210.49(3)	0.91(60)	211.40(60)
$26H_6-I_7$	216.88(4)	0.43(30)	217.31(30)
$27H_6-I_7$	196.02(3)	0.57(40)	196.59(40)
$28H_6-I_7$	288.80(3)	0.62(45)	289.42(45)
$29H_6-I_7$	151.92(3)	0.96(70)	152.88(70)
$30H_6-I_7$	138.96(3)	1.22(90)	140.18(90)

states), \mathbf{S}_1 the spin of the core electron, \mathbf{R} the angular momentum of H_2^+ (exclusive of spins), and $\hat{\rho}$ the direction of the internuclear axis. The hyperfine coupling constants b , c , and d depend on the wave function of H_2^+ and have been calculated elsewhere.¹⁶ The second term in Eq. (18), H_{MS} , is

$$H_{\text{MS}} = \frac{\alpha^2 \mathcal{R}}{r^3} [-0.5 \mathbf{L} \cdot \mathbf{S}_2 + \mathbf{L} \cdot \mathbf{S}_1 + \mathbf{S}_1 \cdot (1 - 3\hat{\mathbf{r}}_2\hat{\mathbf{r}}_2) \cdot \mathbf{S}_2], \quad (20)$$

and represents the magnetic interactions between the core and the Rydberg electron in the approximation that the shape and size of the core wave function may be neglected.¹⁷ The final term in Eq. (18), where $S = S_1 + S_2 = 1, 0$, represents the possible influence of a finite exchange energy. V_x has been shown to be very small for $L \geq 4$ levels.¹⁵

The magnetic fine structure of the high- n states studied here is simplified in some respects, when compared to the $n = 10$ states where it has been studied previously. The contributions of both the exchange energy and of H_{MS} decrease approximately as n^{-3} , so they can be safely neglected in the range of n and L studied here, leaving only the structure produced by H_{HFS} . On the other hand, since the electric fine structure also shrinks approximately as n^{-3} , the structure due to H_{HFS} is no longer

much smaller than the electric fine structure for these high- n states, and this introduces some new complications. Figure 4, for instance, illustrates both the electric and magnetic fine structure for two typical cases.

In order to evaluate the structure produced by H_{HFS} , we take basis states which are eigenstates of $\mathbf{N} = \mathbf{R} + \mathbf{L}$, and $\mathbf{F}_c = \mathbf{I} + \mathbf{S}_1$, combined to form eigenstates of the angular momentum $\mathbf{J}_1 = \mathbf{N} + \mathbf{F}_c$. The total angular momentum of the system is actually $\mathbf{J} = \mathbf{J}_1 + \mathbf{S}_2$, but the structure is virtually unchanged if \mathbf{S}_2 is ignored (exactly unchanged in the approximation that H_{MS} and V_x are ignored). The first and largest term of H_{HFS} is diagonal in this basis, and gives the splitting of $1.5(b+c/3)$ between the two eigenstates of F_c . In many ways, it is more appropriate to think of this part of the MFS as a part of the "core energy" in addition to the vibration and rotational energy. Then one may view Figs. 4(a) and 4(b) as each illustrating the members of two Rydberg series, one bound to the $(0,1,3/2)$ state of H_2^+ and the other bound to the $(0,1,1/2)$ state. The expectation value of the next two terms in H_{HFS} in the chosen basis set gives a first estimate of the MFS, labeled $E^{(1)}$ in Fig. 4. However, H_{HFS} also has off-diagonal matrix elements which influence the structure significantly. These off-diagonal matrix elements, which satisfy the selection rules $\Delta J_1 = 0$, $\Delta F_c = 0, \pm 1$, and $\Delta N = 0, \pm 1, \pm 2$, have the effect of mixing the various states of common J_1 in Fig. 4, thus pro-

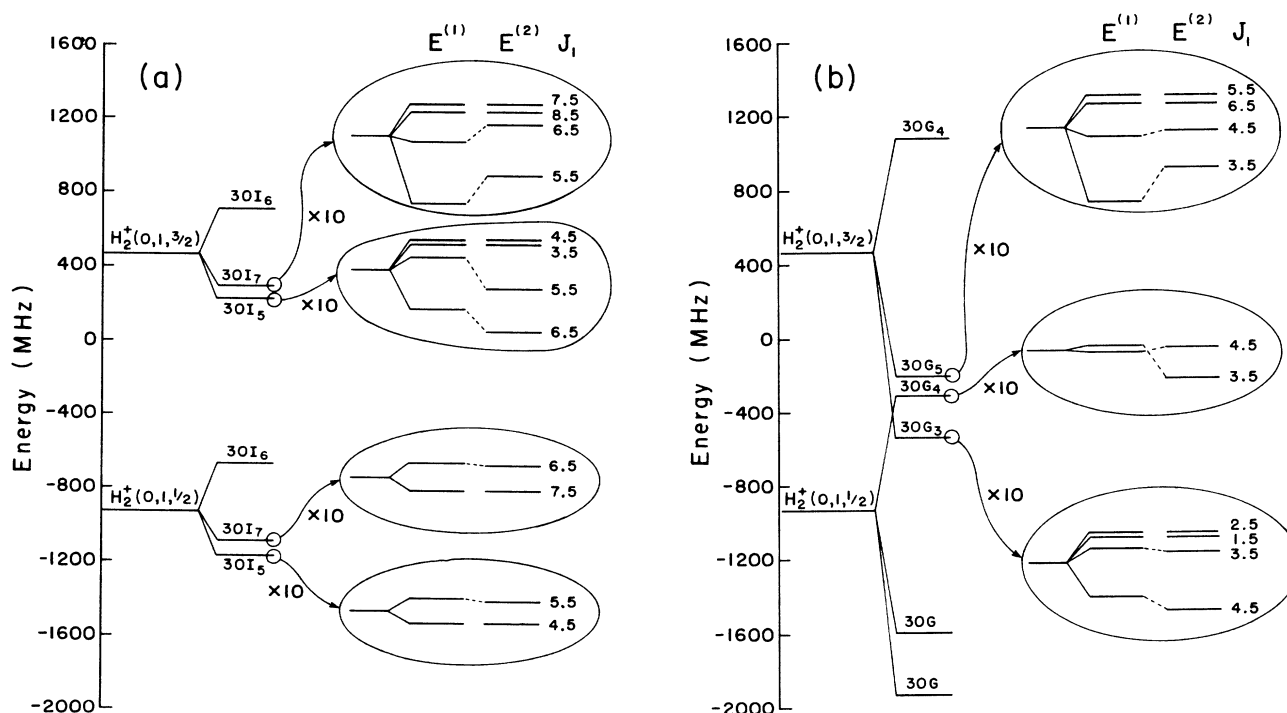


FIG. 4. Illustration of the predicted magnetic fine structure of a representative set of Rydberg levels: (a) the 30I manifold, and (b) the 30G manifold. Each diagram shows the contributions of different elements of the total Hamiltonian, from left to right: the sum of core and hydrogenic energies (the dipole hyperfine structure energy is included as part of the core energy), the contribution of the EFS Hamiltonian [Eq. (1)], and the first-order magnetic fine structure $E^{(1)}$ which splits states of different J_1 , $J_1 = \mathbf{N} + \mathbf{F}_c$. Finally, the effect of the magnetic-fine-structure Hamiltonian in second order $E^{(2)}$ is shown. The latter two contributions are shown on an expanded scale. In both (a) and (b) the close proximity of different magnetic hyperfine levels allows mixing between states that have the same J_1 . In (a) near degeneracies that occur for all large L are demonstrated, while (b) demonstrates how perturbations occur when core splitting and EFS energies are comparable in size.

ducing the energy shifted states labeled $E^{(2)}$.

The most significant of these second-order energy shifts are of two types, as illustrated in Figs. 4(a) and 4(b). The more general case, illustrated in Fig. 4(a), occurs when the energy difference between the $N=L\pm 1$ electric-fine-structure levels becomes comparable to the first-order magnetic-fine-structure energies $E^{(1)}$. Under these circumstances, states which have the same J_1 will show significant second-order energy perturbations [as illustrated in Fig. 4(a)]. Note that for each case of interest, the states with $N=L\pm 1$, only two hyperfine states show significant second-order perturbations, those with $F_c = \frac{3}{2}$ and $J_1 = L \pm \frac{1}{2}$.

The second case of significant second-order energy perturbations occurs when the $F_c = \frac{1}{2}$, $N=L$ state is nearly degenerate with the $F_c = \frac{3}{2}$, $N=L\pm 1$ states. A typical example is illustrated in Fig. 4(b). Since this type of mixing requires an "accidental" near equality of electric fine structure and core hyperfine structure energies, it occurs less frequently than the case illustrated in Fig. 4(a). Note that in this case also it is only the $J_1 = L \pm \frac{1}{2}$ states which are strongly perturbed.

It is precisely the energy shifts due to the type of near degeneracies illustrated in Figs. 4(a) and 4(b) which are responsible for the widely spaced substructure visible in the resonance lines of Fig. 3. Were it not for this type of perturbation, all six of the resonance components contributing to a single such EFS transition (the strongest transitions satisfy the selection rule $\Delta J_1 = \Delta N$, $\Delta F_c = 0$) would be very close to one another. The large resonance component seen in both Figs. 3(a) and 3(b) is expected to contain the four resonances that are not affected by such perturbations. One may then expect that this large peak would give a good estimate of the spinless "EFS" interval.

The MFS pattern predicted by the interactions of Eq. (19), including the off-diagonal perturbations, gives the predicted spectrum of EFS transitions illustrated in Fig. 3 by the stick diagrams. The pattern of the data is quite well reproduced in all cases, although the observed positions of the strongly perturbed lines appear to differ from the predictions by a few tenths of a megahertz, as shown. The reason for this discrepancy is that, due to the mixings, the strongly perturbed levels suffer slightly different Stark shifts than the other levels. Their relative positions in the resonance are thus altered. The small electric fields that are required to produce the observed (relative) shifts are consistent with estimates of stray electric fields thought to exist within the rf region (see below).

The electric-fine-structure intervals were extracted from the data by fitting the spectral lines to a superposition of two-level resonance line shapes¹⁷ whose relative transition energies were calculated from Eq. (19). Because of the differential Stark shifts that were mentioned above, the positions of the two strongly perturbed MFS components were allowed to float in the fit and only the four relatively unperturbed components were used to determine the EFS interval. The relative heights of the six components were taken to be proportional to the statistical weight $(2J_1 + 1)$ of the initial state in the transition, and the common intensity, time of flight, and power

parameters, as well as the EFS interval, were adjusted in the fit. The smooth curves in Fig. 3 are examples of the resulting fits, which were quite acceptable. The statistical errors of the fitted EFS interval are shown in Table V. They are generally smaller than the systematic errors, which are discussed below.

B. Electric fields

By far the most significant systematic error in this experiment is the possible presence of stray electric fields within the microwave interaction region. Previous experimental experience with a similar apparatus¹⁷ would suggest that fields in the range of 0–100 mV/cm might be present, even in the nominally field-free and magnetically shielded interior of the interaction region. These fields can be produced either by imperfect magnetic shielding, which leads to motional electric fields, or by buildup of charges on nominally conducting surfaces. Since the Stark shift rates of these high- n transitions are quite large [approximately equal to 10^3 MHz/(V/cm)²], it was essential to obtain experimental evidence about the size of any such fields that were present during the experiment. We used three techniques, of varying utility, to do this.

The first method was to deliberately impose a uniform external electric field in the interaction region by applying a dc potential to the center conductor of the transmission line which forms the interaction region. This field could, to a certain extent, compensate for any other fields which were already present along the path of the fast beam. When the position of one of the high- n EFS resonances was measured as a function of this dc potential, it did not show a simple quadratic shift, as would be expected in the absence of other fields, but instead showed a minimum shift for a potential of -0.4 V with a quadratic dependence on either side. This would suggest that another field, a "stray" field, approximately the same size as that produced by the 0.4-V potential (approximately equal to 20 mV/cm) was present in the interaction region from other causes. Unfortunately, the stray electric field is unlikely to be uniform throughout the interaction region, nor is it precluded from having polarization perpendicular to the applied field. For these reasons it is certain that the compensation of the stray fields by the uniform external field is only partial. Nevertheless, this method is relatively simple and should give at least an order of magnitude estimate of the stray field, unless its polarization is completely orthogonal to the applied field.

A second method of estimating possible stray electric fields is to compare the observed EFS intervals, particularly for the $n=26, 27, 29$, and 30 states [which are not greatly perturbed by the $(0,3)n=16$ states], with the predictions of the polarization model, and to see whether any differences could be accounted for by a possible stray electric field. The raw experimental numbers, shown in Table VI, are rather more precise than the HOPM predictions, also shown, and are in generally good agreement to within the theoretical error bars that are calculated from Eq. (14). The calculated quadratic Stark shift coefficient for each interval is also shown in Table VI. A somewhat more sensitive test can be obtained by subtracting the two intervals which share initial and final L .

Since this difference is independent of the *scalar* structure factors of both levels, which contain most of the theoretical error, this comparison gives the most precise check for possible Stark effects, especially for the $H-I$ intervals. The measured intervals are entirely consistent with zero stray electric field, and would be inconsistent with stray fields larger than about 30 mV/cm. This comparison thus serves to set a limit on the magnitude of possible stray electric fields.

A third method, which was used on one occasion, was to measure the position of one additional transition, the $(0,1)30H_6-(0,1)30I_6$, which is mildly forbidden compared to the other observed transitions. When combined with the measured position of the $(0,1)30H_6-(0,1)30I_7$ transition, the new measurement gives a determination of the splitting between the $30I_6$ and $30I_7$ states. The results of these measurements, corrected for Doppler shifts but without any Stark shift corrections, are

$$30H_6-30I_6: 565.09(11) \text{ MHz}$$

$$30H_6-30I_7: \underline{138.96(3) \text{ MHz}}$$

$$30I_6-30I_7: 426.13(11) \text{ MHz} .$$

According to the polarization model, this interval is predicted to be 421.6(4) MHz, where the quoted error is due to a conservative assumption of 0.1% uncertainty in the quadrupole moment of H_2^+ . Given the calculated Stark shift rate for this interval [7400 MHz/(V/cm)²] the difference between measured and calculated intervals may be attributed to a stray electric field of 24.6(12) mV/cm, rms, by far the most precise estimate of stray fields. Unfortunately, this test was carried out only once, and there is no guarantee that the stray fields are constant in time.

From these three independent lines of evidence, it appears fair to conclude that there *are* stray electric fields present in the microwave interaction region and that their size is estimated to be 25 ± 10 mV/cm (rms). Based on this estimate, each of the measured high- n EFS intervals were corrected for the Stark shifts which are presumed to have been present when the interval was measured. These corrections are shown in Table V. The uncertainty in this correction, due to uncertainty in the stray field size, is the dominant experimental error in the measured fine-structure intervals. It should also be emphasized that the primary objective in this experiment is to measure the *perturbations* of the EFS because of the

TABLE VI. Comparison between raw experimental line centers for each of 16 $n \neq 28$ fine-structure intervals and the predictions of the polarization model. Shown for each interval is the calculated quadratic Stark shift coefficient c in MHz/(V/cm)², the experimental line centers and the calculated transition frequencies, both in MHz, and the calculated square of the electric field, in (V/cm)², which would cause experiment and theory to agree exactly. Significant nonzero values of $|E|^2$ may be evidence of stray electric fields within the spectroscopy region. The numbers in parentheses denote one standard deviation error estimates.

Interval	c	ν_0^{fit}	ν_0^{HOPM}	$ E ^2$
$26G_3-H_4$	-330	840.00(6)	845(13)	0.015(39)
$26G_5-H_6$	-470	552.68(3)	557(13)	0.009(28)
difference	140	287.32(7)	287.6(12)	-0.002(9)
$26H_4-I_5$	-520	325.21(5)	326.6(19)	0.0027(36)
$26H_6-I_7$	-700	216.88(4)	218.1(18)	0.0017(26)
difference	180	108.33(6)	108.45(17)	-0.0007(7)
$27G_3-H_4$	-440	754.63(7)	759(12)	0.010(27)
$27G_5-H_6$	-610	505.13(3)	509(12)	0.006(20)
difference	180	249.50(8)	249.7(11)	-0.001(6)
$27H_4-I_5$	-680	291.30(3)	292.7(17)	0.0020(25)
$27H_6-I_7$	-920	196.02(3)	197.7(16)	0.0018(17)
difference	240	95.28(4)	95.06(14)	0.0009(6)
$29G_3-H_4$	-730	599.79(11)	604(10)	0.006(14)
$29G_5-H_6$	-1020	381.26(3)	385(9)	0.004(9)
difference	290	218.53(12)	218.8(9)	-0.001(3)
$29H_4-I_5$	-1140	232.39(4)	233.8(14)	0.0012(12)
$29H_6-I_7$	-1540	151.92(3)	153.4(13)	0.0010(8)
difference	400	80.47(5)	80.47(11)	0.0000(3)
$30G_3-H_4$	-930	545.04(6)	548.9(88)	0.004(9)
$30G_5-H_6$	-1300	353.24(3)	356.8(85)	0.003(7)
difference	370	191.80(7)	192.1(9)	-0.001(2)
$30H_4-I_5$	-1460	210.49(3)	212.2(12)	0.0012(8)
$30H_6-I_7$	-1970	138.96(3)	140.7(12)	0.0009(6)
difference	510	71.53(4)	71.51(10)	0.0000(2)

(0,1) $n=28$ (0,3) $n=16$ coincidence. The accuracy of the polarization model predictions of unperturbed EFS is much more easily tested in other experiments.¹ Thus, the reliance which is placed on the theory in estimating possible stray fields is acceptable within the context of the present experiment.

IV. ANALYSIS OF SERIES MIXING

Even a cursory examination of the measured fine structure intervals shown in Table V reveals the large perturbation which occurs at $n=28$. Figure 5 shows the (0,3)16 L_N levels which are responsible for these perturbations. The primary couplings between the two manifolds satisfy the selection rules $\Delta N=0, \Delta L=0$. The $n=16$ levels lie just above the $n=28$ levels and so when coupled to them have the effect of shifting all of the high- L $n=28$ levels downward in energy. Since the size of the perturbation decreases with L , as the coupling decreases, all of the $n=28$ EFS intervals are increased, as Table V confirms.

In order to test the theoretical predictions of the level perturbations, we must first determine the precise value of the shift in each EFS interval at $n=28$. The $n=26, 27, 29$, and 30 measurements of each interval appear to fall on smooth curves. Extrapolating these curves to $n=28$ gives an estimate of the intervals that would be observed in the absence of the strong perturbation. Subtracting the extrapolated value at $n=28$ from the actual measured interval gives an experimental estimate of the perturbation. The value obtained for the $n=28$ intercept is not very sensitive to the method of extrapolation, although the quality of the fit improves as more care is taken, and this increases confidence in the intercept. Table VII illustrates the results of several extrapolation methods. The simplest method, fitting to the function A/n^3 , gives a rms deviation of about 4 MHz in the fits. This function, however, fails to account for the small but non-negligible perturbations of the $n \neq 28$ levels as they approach the (0,3) $n=16$ perturber. One way to account for this is to fit the $n \neq 28$ intervals to the function

$$v_0(n) = (A + C/\Delta E_n)/n^3,$$

where ΔE_n is the difference in zeroth-order energies be-

tween the (0,1) n and (0,3)16 Rydberg levels,

$$\Delta E_n \cong 109\,707/n^2 - 139.684 \text{ cm}^{-1}.$$

This gives a much better fit, with a correspondingly more precise intercept. Adding a third parameter, proportional to n^{-5} , further improves the quality of the fit. An alternative method of dealing with the slight perturbations of the $n \neq 28$ levels is to rely on calculations of these small shifts (≤ 20 MHz). This results in the fit labeled 4 in Table VII. Yet another, completely independent way to estimate the "unperturbed" $n=28$ interval would be to rely on polarization model calculations, but these are much less precise than the measurements, as also shown in Table VII. All of the extrapolation methods give general agreement for the value of the "unperturbed" $n=28$ intercept. If we take function 4 to be the most reliable estimate, and subtract those extrapolated $n=28$ intervals from the measured intervals, we obtain the experimental measurements of energy shifts shown in Table X. Notice that the shift can be inferred in all cases to a precision of better than 1%.

Theoretical calculation of the large $n=28$ perturbations might begin with the second term of Eq. (2), which would give for the energy shift of each $n=28$ EFS level

$$\delta E = \frac{|\langle 28 | V_{\text{pol}} | 16 \rangle|^2}{E^0(28) - E^0(16)}. \quad (21)$$

It is evident from Fig. 5, however, that the difference of zeroth-order energies is not a very precise estimate of the energy difference between the two states being mixed; the EFS of both levels is comparable to the zeroth-order energy difference. Consequently, Eq. (21) gives only a very crude estimate of the expected shift. We speculated, in Sec. II, that the Rydberg state eigenvalues might be correctly obtained, to all orders in V_{pol} , by diagonalizing the effective Hamiltonian

$$H_{\text{eff}} = H_0 + V_{\text{pol}}$$

in the space of all Rydberg levels. Of course this is an infinite matrix, so its eigenvalues can only be obtained approximately. The simplest approximation technique would be to diagonalize the submatrix including only the

TABLE VII. Estimates of the "unperturbed" value of $n=28$ fine-structure intervals. Estimates (1)–(4) are based on extrapolations of experimental numbers from $n=26, 27, 29$, and 30 . For each method of fitting, the $n=28$ intercept and the rms deviation from the fitted curve is shown. Estimate (5) is the calculated interval based on the HOPM polarization potential, as obtained from Tables II and IV. All results are in MHz. The numbers in parentheses denote one standard deviation error estimates.

Method	$G_3 - H_4$	$G_5 - H_6$	$H_4 - I_5$	$H_6 - I_7$
(1) A/n^3	673.3(16)	443.4(41)	260.8(4)	174.3(9)
rms deviation	3.63	10.72	0.97	2.43
(2) $[A + C/\Delta E(n)]/n^3$	671.4(9)	438.2(18)	260.21(17)	172.92(40)
rms deviation	1.23	2.62	0.25	0.62
(3) $(A + C/\Delta E_n)/n^3 + B/n^5$	672.44(5)	440.37(20)	260.42(3)	173.42(7)
rms deviation	0.06	0.20	0.03	0.09
(4) $A/n^3 + B/n^5 + \Delta v^{\text{calc}}$	672.40(8)	440.51(8)	260.41(12)	173.42(16)
rms deviation	0.10	0.10	0.13	0.15
(5) HOPM theory	676(11)	444(10)	261.1(15)	174.2(15)

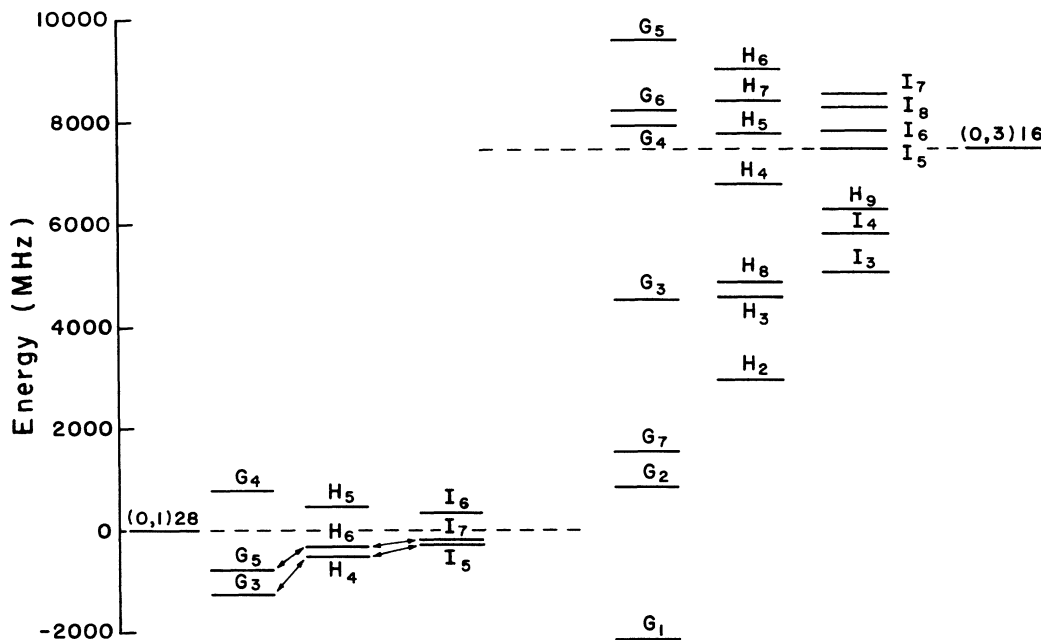


FIG. 5. Level diagram showing the $(0,1)28L_N$ levels measured here, and the nearby $(0,3)16L_N$ levels which perturb them. All the levels are shown in their calculated "unperturbed" positions. The most important couplings, as discussed in the text, are between states that share the same L and N . The fine-structure intervals which are measured in this experiment are shown by arrows.

nearly degenerate levels. An improved approximation is obtained by including, on the diagonal of this submatrix, the second-order polarization energies due to coupling with all other Rydberg states.¹¹ We adopt this improved procedure.

The energies of the $n=28$ Rydberg levels in question, excluding the 28–16 coupling, have already been calculated and are shown in Tables II and IV. For the $(0,3)16$ states, the first-order structure is slightly more complicated since angular momentum factors no longer prevent contributions from terms in the HOPM potential proportional to $P_4(\cos\theta)$. We find, as the generalization of Eq. (17a),

$$\langle \psi_R | V_{\text{pol}} | \psi_R \rangle = A_0 + A_2 \langle RLN | P_2(\cos\theta) | RLN \rangle + A_4 \langle RLN | P_4(\cos\theta) | RLN \rangle, \quad (22)$$

where A_0 , A_2 , and A_4 are given by the expectation value of the appropriate terms in Eq. (13). Table VIII gives the calculated values of each of these structure factors for the $(0,3)16L$ levels with $2 < L < 8$. In each case, the estimated error, inferred from the convergence of successive terms in the polarization potential, is taken to be one half of the smallest V_s . The first-order polarization energies of any of the $n=16$ states involved in the present mixing may be calculated from these structure coefficients. The second-order polarization energies, obtained as in Table IV, have also been calculated for the states of interest, and are shown in Table IX.

The possible couplings between the states illustrated in Fig. 5 must satisfy $\Delta N = 0$ and $\Delta L = 0, \pm 2, \pm 4$. When the appropriate matrix elements are calculated, however, the $\Delta L = 0$ couplings are found to be by far the most significant. In fact, of all the possible $\Delta L \neq 0$ couplings involving the six $n=28$ levels of interest, only two particular couplings give shifts that are significant at the level

TABLE VIII. Structure factors for the $(0,3)16L$ states of H_2 , calculated with the polarization potential, including terms to order r^{-6} (HOPM). The energy of each Rydberg level is given by $E[(\nu, R)16L_N] = A_0 + A_2 \langle RLN | P_2 | RLN \rangle + A_4 \langle RLN | P_4 | RLN \rangle$. The numbers in parentheses denote one standard deviation error estimates.

States	A_0 (MHz)	A_2 (MHz)	A_4 (MHz)
$(0,3)16D_N$	-11 000(38 000)	-200 000(20 500)	-31 000(5500)
$(0,3)16F_N$	-7400(680)	-70 100(360)	-1800(100)
$(0,3)16G_N$	-2134(50)	-31 480(27)	-261(7)
$(0,3)16H_N$	-767(7)	-16 830(4)	-58(1)
$(0,3)16I_N$	-324.8(14)	-10 051.8(7)	-16.8(2)
$(0,3)16K_N$	-154.9(3)	-6 485.6(2)	-5.81(5)
$(0,3)16L_N$	-80.67(10)	-4429.02(5)	-2.25(1)

TABLE IX. Calculated perturbations of $(0,1)28L_N$ levels due to mixing with $(0,3)16L_N$ levels. For each pair of levels, the unperturbed levels positions are tabulated in zeroth, first, and second order in V_{pol} , where $E^{(2)}$ excludes the contribution of the nearly degenerate levels. The matrix element of V_{pol} between each pair of levels is shown in column 5, and column 6 has the $n=28$ level shifts, which were calculated using Eq. (23) and the total energy difference. All values are in MHz. The numbers in parentheses denote one standard deviation error estimates.

Interval	E^0	E^1	E^2	$\langle V_{\text{pol}}^{\text{HOPM}} \rangle$	$\delta\nu(28)$
$(0,3)16G_3$ $(0,1)28G_3$	7465(30) 0.0 ^a	-2930(52) -1228(11)	-65(1) -7.8(5)	1600.8(11)	-418.4(40)
$(0,3)16G_5$ $(0,1)28G_5$	7465(30) 0.0	2180(46) -821.0(10)	-168.6(9) -7.8(3)	2586.9(22)	-612.9(31)
$(0,3)16H_4$ $(0,1)28H_4$	7465(30) 0.0	-676.6(70) -558.6(15)	-19.45(3) -1.11(3)	893.95(17)	-107.5(5)
$(0,3)16H_6$ $(0,1)28H_6$	7465(30) 0.0	1530.4(64) -383.5(15)	-42.47(6) -1.5(1)	1311.97(30)	-180.4(6) ^b
$(0,3)16I_5$ $(0,1)28I_5$	7465(30) 0.0	-80.2(14) -298.0(3)	-6.128(2) -0.215(3)	538.89(4)	-37.64(15)
$(0,3)16I_7$ $(0,1)28I_7$	7465(30) 0.0	1026.5(13) -210.4(3)	-13.246(6) -0.40(1)	742.07(6)	-64.49(22) ^c

^aFor convenience, the zeroth-order energy of $(0,1)n=28$ levels is set to zero.

^bThis number includes a calculated shift of 0.4 MHz caused by coupling to the $(0,3)16F_6$ state.

^cThis number includes a calculated shift of -1.57 MHz caused by coupling to the $(0,3)16G_7$ states.

of experimental precision. These two small shifts are given specifically in Table IX, where they apply.

Aside from the above effects, the important mixing is predicted to occur in pairs of two levels, each sharing both L and N . Table IX shows the calculated matrix element of $V_{\text{pol}}^{\text{HOPM}}$ between each such pair of levels, with an error estimate derived from Eq. (14). Also shown are the best estimates of the energies of both levels of the pair, before mixing. The error in the energy difference between the two levels is due in part to the uncertainty in the 1-3 (calculated) rotational splitting of H_2^+ , $288.861(1) \text{ cm}^{-1}$, contributing an error of ± 30 MHz to the energy differences. This is the dominant error in the calculated shifts of $L > 4$ states. Other contributions to the error in the energy difference come from the estimated uncertainties in the calculated first and second order polarization energies, and are found from Eqs. (14) and (15).

The degree of mixing of Rydberg states of the two series is sufficiently large that a perturbative estimate of the mixing and shift would not be precise enough for comparison with the data. Since we are dealing with only pairs of coupled levels, however, we can explicitly diagonalize the 2×2 matrices which occur and find

$$\delta E(28) = \Delta E / 2 - [(\Delta E / 2)^2 + V^2]^{1/2}, \quad (23)$$

where ΔE is the estimated energy splitting between the two states, and V is the matrix element of V_{pol} between them. The error in the calculated shift δE is calculated by propagating the errors in ΔE and V . The mixing

coefficient between the two series, by amplitude, is given by

$$\epsilon = V / \Delta E$$

which is as large as 0.29 for one case.

Table X compares the calculated and observed shifts in the four EFS intervals studied. Excellent agreement is observed in all cases. This confirms that, at least for these states, the degree of mixing between nearly degenerate high- L Rydberg series is very well predicted by the polarization model. This result supports the hypothesis that the correct Rydberg energy is found by diagonalizing $H_0 + V_{\text{pol}}$; the agreement would be completely unacceptable if Eq. (21) were used directly to calculate the energy shifts.

TABLE X. Comparison between observed and predicted perturbations of the four fine-structure intervals. Column 2 gives the observed shift of the interval at $n=28$, derived from subtracting the $n=28$ extrapolated value (Table VII) from the measured $n=28$ interval (Table V). Column 3 gives the shift predicted from the matrix element of $V_{\text{pol}}^{\text{HOPM}}$, as tabulated in Table IX. Column 4 gives the difference between experiment and theory. All values are in MHz. The numbers in parentheses denote one standard deviation error estimates.

Interval	$\delta\nu^{\text{expt}}$	$\delta\nu^{\text{theor}}$	$\delta\nu^{\text{expt}} - \delta\nu^{\text{theor}}$
G_3-H_4	314.3(2)	311.0(49)	3.3(49)
G_5-H_6	432.0(3)	432.5(36)	-0.5(36)
H_4-I_5	70.5(5)	69.9(4)	0.6(6)
H_6-I_7	116.0(5)	115.9(6)	0.1(9)

V. CONCLUSION

We have observed large- n ($26 \leq n \leq 30$) fine-structure transitions in molecular hydrogen, using a new experimental method. The transitions show hyperfine structure which is well described by an *ad hoc* hyperfine Hamiltonian. We have experimentally measured, to 1%, the effect of series mixing between the nearly degenerate $(0,1)n=28$ and $(0,3)n=16$ fine-structure levels, which manifests itself in large perturbations of the $n=28$ fine-structure intervals. The observed perturbations are completely consistent with the predictions of an *a priori* polarization model. In order to obtain this agreement, however, it is necessary to assume that the correct eigenvalues are calculated by diagonalizing an effective Hamiltonian which includes the zeroth-order Hamiltonian and the polarization potential. We provide some justification for this assumption. The good agreement also indicates that short-range interactions are negligible for the states studied here.

ACKNOWLEDGMENTS

This work was supported by the National Science Foundation under Grant No. PHY87-09797. The authors are indebted to David Bishop for providing results of calculations prior to publication. One of us (S.R.L.) wishes to acknowledge the hospitality of the Joint Institute for Laboratory Astrophysics at the University of Colorado, while receiving support from the JILA Visiting Fellow Program, where much of this work was carried out.

APPENDIX

The coefficients of the various terms in the polarization potential depend on electrical properties of the free H_2^+ ion. Most of these have been calculated explicitly as a function of the internuclear separation ρ , and then averaged over the rovibrational wave function appropriate to

a given (ν, R) state.¹² The values used for the calculations of this paper for the (0,1) and (0,3) states are shown below. In the case of the adiabatic quadrupole polarizabilities, only the *electronic* polarizabilities is used, in contrast to Ref. 2. Matrix elements of V_{pol} between Rydberg series bound to these two different states would require off-diagonal matrix elements of these functions of ρ . However, since the rovibrational functions for (0,1) and (0,3) are only slightly different, we have approximated the off-diagonal matrix elements of the core parameters as the geometric mean of the diagonal matrix elements for the two core states. The nonadiabatic dipole polarizabilities have not been calculated for the (0,3) state. We used the (0,1) values as an approximation, and they are shown enclosed in parentheses.

Core property	(0,1)	(0,3)
quadrupole moment (ea_0^2)		
Q	1.642 57	1.662 56
adiabatic dipole polarizability (a_0^3)		
α_S	3.180 88	3.229 11
α_T	4.027 31	4.125 83
hexadecapole moment (ea_0^4)		
ϕ	2.0192	2.0698
Nonadiabatic dipole polarizability (a_0^4/e^0)		
β_S	6.84	(6.84)
β_T	12.49	(12.49)
Adiabatic quadrupole polarizabilities (a_0^5)		
C_0	24.066	24.451
C_1	5.118	5.247
C_2	0.420	0.434
Adiabatic dipole-octupole polarizabilities (a_0^5)		
E_1	8.69	9.02
E_2	32.68	33.68

¹W. G. Sturuss, E. A. Hessels, P. W. Arcuni, and S. R. Lundeen, Phys. Rev. Lett. **61**, 2320 (1988).

²W. G. Sturuss, E. A. Hessels, P. W. Arcuni, and S. R. Lundeen, Phys. Rev. A **38**, 135 (1988).

³Richard J. Drachman, Phys. Rev. A **26**, 1228 (1982); **31**, 1253 (1985).

⁴U. Fano, Phys. Rev. A **2**, 353 (1970).

⁵E. E. Eyler, Phys. Rev. A **34**, 2881 (1986).

⁶Richard J. Drachman, Phys. Rev. A **37**, 979 (1988).

⁷L. Wolniewicz and J. D. Poll, Mol. Phys. **59**, 953 (1986).

⁸E. E. Eyler and F. M. Pipkin, Phys. Rev. A **27**, 2462 (1983).

⁹The terms of order ϵ can be shown to introduce small corrections to the coefficients of the polarization potential, which are negligibly small for the purposes of this paper.

¹⁰S. A. Blundell and S. R. Lundeen (unpublished).

¹¹I. Lindgren and J. Morrison, *Atomic Many Body Theory* (Springer-Verlag, New York, 1982), Chap. 9.

¹²David M. Bishop (private communication). Values used are similar to those reported in Tables 2 and 3 of Chem. Phys. Lett. **134**, 283 (1987), except that the rovibrational averages correspond to the (0,1) and (0,3) states, instead of the (0,0) state used there.

¹³W. G. Sturuss, P. E. Sobol, and S. R. Lundeen, Phys. Rev. Lett. **54**, 792 (1985).

¹⁴K. B. MacAdam, R. G. Rolfes, and D. A. Crosby, Phys. Rev. A **24**, 1286 (1981).

¹⁵W. G. Sturuss, E. A. Hessels, and S. R. Lundeen, Phys. Rev. Lett. **57**, 1863 (1986).

¹⁶R. P. McEachron, C. J. Veenstra, and M. Cohen, Chem. Phys. Lett. **59**, 275 (1978); Roger D. Ray and Phillip R. Certain, Phys. Rev. Lett. **38**, 824 (1977).

¹⁷E. A. Hessels, W. G. Sturuss, S. R. Lundeen, and David R. Cok, Phys. Rev. A **35**, 4489 (1987).